Theoretical Study of the Impact of Pore Size in TiO_2 Aerogels on Photocatalytic Formaldehyde Decomposition

Fenglei Sun , Xianbo Yu , Junhui Xiang *

Posted Date: 22 May 2024

doi: 10.20944/preprints202405.1440.v1

Keywords: HCHO; TiO2 aerogel; pore size; photocatalysis; oxygen pressure; decomposition

Article

Theoretical Study of the Impact of Pore Size in TiO_2 Aerogels on Photocatalytic Formaldehyde Decomposition

Fenglei Sun, Xianbo Yu and Junhui Xiang *

Center of Materials Science and Optoelectronics Engineering, College of Materials Science and Optoelectronics Engineering, University of Chinese Academy of Sciences, Beijing, 100049, China; sunfenglei18@mails.ucas.ac.cn (F.S.); yuxianbo18@mails.ucas.ac.cn (X.Y.).

* Correspondence: xiangjh@ucas.ac.cn (J.X.); Tel: 86-010-6967 1772.

Abstract: Formaldehyde (HCHO), an indoor volatile organic compound, is seriously harmful to human health. Therefore, green and effective decomposition of HCHO is essential. TiO_2 has been employed for the degradation of HCHO via photocatalytic generation of reactive oxygen species (ROS) (O^{2-}, ·OH), yet the low specific surface area of crystalline TiO_2 depressed the catalytic performance. Herein, we prepared TiO_2 aerogels with high specific surface area and high porosity by sol-gel method, and added PVA to introduce flexible molecular chains for pore size regulation. The photocatalytic performance test verifies that the pore size of TiO_2 aerogel is one of the important factors for HCHO decomposition. Notably, through the establishment of theoretical model and calculation, we validated that the efficiency of HCHO decomposition is related to the oxygen pressure in the pores of TiO_2 aerogel, and the oxygen pressure is inversely proportional to the pore size. Accordingly, the optimal pore size of TiO_2 aerogel for the photocatalytic HCHO decomposition is 2 nm~10 nm. This study provides a theoretical idea for TiO_2 aerogels in the decomposition reaction of HCHO, which is expected to inspire more breakthroughs in the study of TiO_2 aerogels for green chemistry.

Keywords: HCHO; TiO_2 aerogel; pore size; photocatalysis; oxygen pressure; decomposition

1. Introduction

Indoor air quality (IAQ) is an important factor affecting human health. Formaldehyde (HCHO) is a typical indoor volatile organic compound [1–5], (VOC) that has severe influence on IAQ, which cannot be ignored for the health hazards of occupants. Hence, the treatment of HCHO has attracted much attention. There are many traditional methods for HCHO treatment, such as adsorption purification method [6–10], biological degradation method [11–13], air negative ion technology [14–16], and thermal destruction method [17–19]. However, these methods all have certain deficiencies for poor HCHO treatment effect and easily-triggered secondary pollution. Hence, it is necessary to develop an environmentally friendly method with lower cost and higher efficiency for HCHO purification. In recent years, photocatalytic oxidation method [20–23], has attracted many interests for the advantages of high removal efficiency, low-temperature requirement (room temperature), wide applicability, and no secondary pollution. By using light energy, the organics distributed on the catalyst surface could be easily degraded into non-toxic H_2O and CO_2 [24]. This method has the advantages of high removal efficiency, low temperature requirement (room temperature), wide application range, no secondary pollution, so it has attracted extensive attention and research.

Since the discovery of water molecules decomposition under ultraviolet irradiation on the surface of TiO_2 electrodes by Fujishima Akira in 1972, the theory [25], and application of TiO_2-based photocatalysts in the field of photocatalysis have been further developed after decades, and they have also become ideal materials for photocatalytic decomposition of HCHO [26,27]. Wang et al. [28], prepared TiO_2/C/MnO_2 ternary photocatalyst for visible light degradation of formaldehyde. Huang et al. [29], found that Pd/ TiO_2 complex made of TiO_2 supported with 0.1% Pd as catalyst could

 doi:10.20944/preprints202405.1440.v1

decompose all HCHO into CO_2 and H_2O at room temperature. He et al. [30], found that when Ir/TiO_2 was doped with Na^+, the decomposition rate of HCHO could reach 100%. Studied [31,32], show that nitrogen-doped nano- TiO_2 can broaden its spectral response range. In another work, Liu et al. [33], prepared nitrogen-doped TiO_2 film by sol-gel method to degrade HCHO, and the decomposition rate of HCHO reached 90% within 24 h, showing good stability and reusability. Tompsett et al. [34], modified TiO_2 by nitrogen doping and found that the modified nano TiO_2 had good photocatalytic decomposition performance under the illumination condition of 440 nm wavelength. Although a large number of experiments have been conducted to study the effect of doping ions into TiO_2 on the decomposition of HCHO, and the factors affecting the photocatalytic decomposition of HCHO by TiO_2 have been obtained, few studies have been conducted on the decomposition of HCHO by TiO_2 aerogels, and insufficient theoretical analysis has been conducted. In this study, the factors affecting the decomposition of HCHO by TiO_2 aerogels have been analyzed experimentally and theoretically.

TiO_2 aerogel is a kind of porous inorganic material with high specific surface area and high porosity [35–39]. Due to these structural characteristics, it is commonly used as catalyst directly or the matrix to load catalyst [40–42], which showing a great catalytic performance. At present, there are many methods to prepare TiO_2 aerogels, including sol-gel method [43–47], hydrothermal method [48,49], dry method [50,51], microemulsion method [52,53], precipitation method [54–57], and so on. Among these common strategies, the sol-gel method has received the most widely studied. The pore size and specific surface area of TiO_2 aerogels prepared by sol-gel method are affected by many factors, such as the concentration of precursor solution [58,59], preparation conditions (including temperature [60,61], pH value [62], reaction time [63,64], etc.), additives amount [65], drying ways [66–68], post-treatment modification [69,70], *etc.* However, the pore size of aerogel cannot be accurately regulated by controlling just the concentration of solution [71]. The technology of post-treatment modification is always complicated and requires sufficient strength [72,73], of TiO_2 aerogel. Notably, the introduction of additives during sol-gel process can effectively regulate the pore size distribution range of aerogel. For example, polyvinyl alcohol (PVA) is a polymer with good film-forming and adhesion properties, which is expected to enhance the structural stability of aerogels by doping into the aerogels. By adjusting the concentration and doping mode of PVA, the pore size distribution of aerogel can be precisely controlled, and thus well-designed aerogel with specific pore size could be obtained.

In this study, we combined experiments and theoretical calculations to analyze the effect of pore size on catalytic HCHO decomposition activities for TiO_2 aerogel. As a kind of small molecule organics, HCHO can be degraded rapidly by using TiO_2 aerogels as photocatalysts. Therefore, the development of effective TiO_2-based photocatalysts has become the research focus. However, most of the current studies are experimental exploration, which lacking the sufficient theoretical analysis for the corresponding decomposition process. Herein, we have prepared TiO_2 aerogels with different pore sizes by sol-gel method. Flexible molecular chains were introduced to control the pore sizes of TiO_2 aerogels. The structural characteristics were determined by infrared spectrometer, scanning electron microscope and specific surface area tester. Then, the degradation effect of HCHO was measured by ultraviolet spectrophotometer and gas chromatograph. Since oxygen plays an important role in the decomposition of HCHO by TiO_2 aerogels, the influence of pore size on the decomposition effect of HCHO was obtained by detecting the oxygen pressure in different pore sizes of TiO_2 aerogels. This study provides a theoretical idea for the application of aerogels in the photocatalysis field, which is expected to inspire further breakthroughs in the study of TiO_2 aerogels for HCHO decomposition.

2. Materials and Methods

2.1. Materials and Chemicals

Tetrabutyl titanate ($C_{16}H_{36}O_4Ti$, GR), anhydrous ethanol (C_2H_5OH, AR), acetic acid (CH_3COOH, GR), formamide (CH_3NO, AR), polyvinyl alcohol 1788 ($[C_2H_4O]n$), formaldehyde (HCHO, AR) and tert-butanol ($C_4H_{10}O$, AR) were purchased from Shanghai Macklin Biochemical Technology Co. Ltd.,

 doi:10.20944/preprints202405.1440.v1

Deionized water (H_2O) is ultrapure water (18.2 MΩ/cm) treated by UHP ultra pure water machine. The reagents and raw materials involved in this experiment can be used directly without further post-treatment purification process.

2.2. Experiment Methods

2.5 ml tetrabutyl titanate was mixed with 5 ml anhydrous ethanol stirring for 10 min to prepare solution A. Aqueous solution of 0.5 ml acetic acid and 1 ml polyvinyl alcohol (PVA) was added to 5 ml anhydrous ethanol by stirring for 10 min to prepare solution B. Then, solution B was slowly added to solution A with continuous stirring for 10 min, followed by the addition of 1 ml formamide and gelled after standing for 1 h. The obtained TiO_2 wet gel was placed in the oven and aged at 60 ℃ for 12 h. After that, the as-prepared aerogel was put into 40% tert-butanol aqueous solution for 12 h and repeated 2 times, followed by vacuum freeze-drying at a temperature below -45℃ and a pressure below 0.5 Pa for 24 h. Finally, the TiO_2 aerogel photocatalyst with excellent catalytic performance was obtained by heat treatment at 800 ℃ in a tube furnace for 6 h. During the preparation process, PVA solutions with different mass fractions (0 wt%, 1 wt%, 3 wt%, 5 wt%) were added and named Ti-0, Ti-1, Ti-2, and Ti-3, respectively.

2.3. Photocatalysis Experiment

0.5 g of as-prepared TiO_2 aerogels was placed in an open centrifuge tube, and the blank sample was set as the control group. The centrifuge tube was suspended in a 50 ml volumetric bottle containing 10 ml HCHO aqueous solution with a concentration of 0.1 mol/L. The volumetric bottle was placed under the ultraviolet lamp to irradiate 10 min every 1h for 4h continuously. Taking 0.1ml HCHO aqueous solution to detect the absorption peak of HCHO aqueous solution by gas chromatography for calculating the HCHO concentration change, and the absorbance of HCHO aqueous solution was measured by ultraviolet spectrophotometer to calculate the HCHO concentration in the solution. The photocatalysis experiment was carried out three times to take an average value. Finally, the HCHO degradation efficiency of TiO_2 aerogel was obtained according to the change of HCHO concentration using the following equation:

$$\eta = \frac{c_0 - c}{c_0} \times 100\% \quad (1)$$

Where η is the degree of decomposition of HCHO, c is the tested concentration of HCHO aqueous solution, and c_0 is the initial concentration of HCHO solution.

The formula for calculating the standard uncertainty is:

$$u_A(x) = \sqrt{\frac{\sum_{i=1}^{n}(x_i - \bar{x})^2}{n-1}} \quad (2)$$

$$u_B(x) = \frac{a}{k_u} = \sqrt{u_{B_1}(x)^2 + u_{B_2}(x)^2 + \cdots} \quad (3)$$

$$u(x) = \sqrt{u_A(x)^2 + u_B(x)^2} \quad (4)$$

In formula (2), (3) and (4), $u_A(x)$ is class A standard uncertainty; $u_B(x)$ is class B standard uncertainty, a is a known condition, k_u is an inclusion factor; $u(x)$ is class B standard uncertainty.

2.4. Materials Characterization

Field Emission Scanning Electron Microscope (SEM): The morphology of the materials was analyzed using a Hitachi SU-4800 scanning electron microscope (SEM) from Hitachi, Japan. The operational parameters were set as follows: working voltage of 30kV, electron accelerating voltage of 5kV, working current of 10μA, and working distance (WD) of 8mm. Elemental and content analysis of the catalyst was carried out using X-ray spectrometry (EDS) with a Tecnai G2 F20 S-TWIN model, which is an accessory to the SEM. The test conditions included a working voltage of 30kV, electron acceleration voltage of 15kV, working current of 10μA, working distance (WD) of 15mm, and a scanning time of 120 seconds.

 doi:10.20944/preprints202405.1440.v1

Field Emission Transmission Electron Microscopy (TEM): Transmission electron images were captured under high voltage using a Hitachi-7700 transmission electron microscope (TEM) operating at 120 kV. Additionally, high-resolution transmission electron microscopy (HR-TEM) was conducted at an accelerating voltage of 200 kV.

X-ray diffraction (XRD): The phase structure of the material was characterized using an X-ray powder diffractometer, specifically the Smartlab model from Rigaku. Test parameters included a Cu target (λ = 0.154 nm), tube voltage of 40 kV, tube current of 225 mA, scan rate of 15°-min-1, and a scan range of 2θ = 20° to 80°.

Thermogravimetric analysis (TG): The thermogravimetric-temperature (TG-T) characterization was performed using an HCT-1 integrated thermal analyzer from China. Samples weighing 5-10 mg of TiO_2 aerogel were placed in an alumina crucible and heated to 800°C under air atmosphere conditions with a temperature increase rate of 10°C/min.

Spectroscopic tests: The chemical properties of TiO_2 aerogels were investigated using Fourier transform infrared spectroscopy with a Bruker TENSOR instrument from Germany. The absorption wavelength range of TiO_2 aerogels was measured using a UV-visible spectrophotometer from Japan (UV-3600 Plus). A liquid UV spectrophotometer from Australia (Agilent Cary60) was utilized to measure the absorption wavelength range of formaldehyde aqueous solution. Furthermore, a gas chromatograph from China (GC7920-GTF2ZV) detected the signal peak of formaldehyde.

Specific surface area tester: The specific surface area and pore size distribution of TiO_2 aerogels were determined using a Gemini V specific surface area tester from Micromeritics, USA. Samples weighing between 30mg to 100mg were subjected to N_2 adsorption-desorption tests at a liquid nitrogen temperature of 77K. The test parameters included taking six points in the P/P0 pressure range between 0.05 and 0.3, calculating the cross-sectional area of N_2 molecules as 0.162 nm^2, utilizing the Brunauer-Emmett-Teller (BET) analysis for specific surface area determination, determining the volume of the sample intermediary pores at P/P_0 of 0.985, and employing the Barrett-Joyner-Halenda (BJH) algorithm to ascertain the pore size distribution of the samples of interest.

3. Results

3.1. Structure and Composition Characterization of TiO2 Aerogel

A schematic diagram of the conventional sol-gel method for the preparation of TiO_2 aerogels, which involves the hydrolysis of Ti organic salt solutions, and the condensation process is illustrated in Figure 1. The SEM image (right upper) shows TiO_2 aerogels without PVA exhibit wide pore size distribution and large average pore size. In our approach, illustrated at the bottom of Figure 1, we modify the process by incorporating flexible molecular chains and the resulting material is shown in the SEM image (right bottom). By adding PVA to the hydrolyzed precursor, we were able to achieve TiO_2 aerogels with adjustable pore size through in-situ growth and self-assembly facilitated by -OH bonding. Here, we used the mass fraction of added PVA as a variable to obtain three TiO_2 aerogels named Ti-1, Ti-2, and Ti-3, while the TiO_2 aerogel without PVA named Ti-0.

Preprints.org (www.preprints.org) | NOT PEER-REVIEWED | Posted: 22 May 2024 doi:10.20944/preprints202405.1440.v1

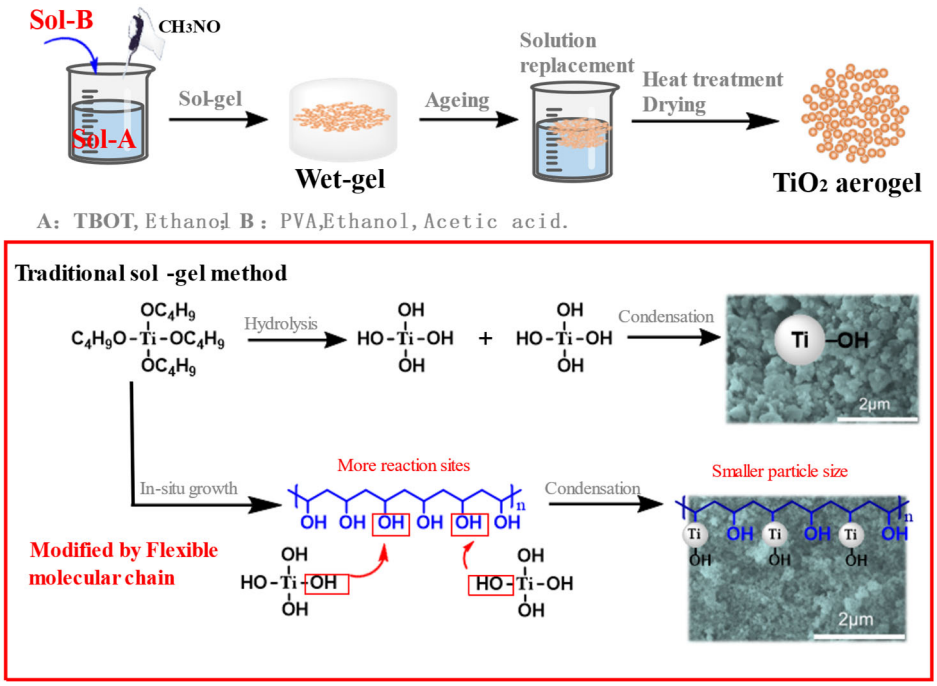

Figure 1. Preparation process and reaction method of TiO_2 aerogel.

To explore the effect of added PVA on the pore size of TiO_2 aerogels, the N_2 adsorption-desorption curves, and pore size distribution curves were investigated. Due to capillary condensation, N_2 molecules undergo condensation and occupy the mesoporous at pressures lower than normal. The process of N_2 adsorption initiates from the pore wall, while N_2 desorption initiates from the orifice. Consequently, there is a disparity between the adsorption and desorption isotherms, resulting in the formation of hysteresis circles. As shown in Figure 2a, Ti-1, Ti-2 and Ti-3 showed significant hysteresis circles in the relative pressure range of 0.4-1.0, indicating that the pore size distribution was concentrated in the mesoporous region in the samples. However, Ti-0 shows no significant hysteresis circles, indicating larger pore size and fewer mesopores. Then, the pore size distribution curves of the sample were analyzed, and noticed that the average pore size of TiO_2 aerogels gradually increased with the increase of PVA content. The average pore size of Ti-1, Ti-2 and Ti-3 are 7.3 nm, 12.9 nm and 48.6 nm, respectively, and all were mesoporous. However, the average pore size of Ti-0 without PVA is 64.6 nm, which belongs to the macropore. It can be seen that by adding a small amount of PVA, the hydroxyl group on this flexible polymer chain will react with TBOT, making TiO_2 particles dispersed evenly, which is conducive to reducing the average pore size of TiO_2. It is worth noting that the pore volume displayed a noticeable decrease as the PVA content increased (as shown in Figure 2b and Table S_1). This can be explained by the fact that besides bonding with the hydrolyzed precursor, the PVA molecular chains that not react completely will also intertwine with each other and occupy the aerogel's pores. Simultaneously, during the gelation process, the diffusion rate and distribution uniformity of PVA in solution will directly affect the structure of the gel. Excessive local crosslinking density arises from uneven diffusion when an excessive amount of PVA is present, subsequently impacting both pore structure and size distribution within the aerogel. In addition, due to its abundant hydroxyl groups and strong affinity with water molecules, PVA acts as an ice nucleating agent that modulates ice crystal growth and regulates pore size [74]. After high-temperature heat treatment, the PVA in the pores was thermally decomposed, yet the pore size became larger and the number of pores was greatly reduced, resulting in a decrease in the pore volume. The distribution of pore size distributions of Ti-1, Ti-2 and Ti-3 are clearly observed in Figure 2b, which concentrates on 2-10 nm, 10-20 nm and 20-50 nm. The addition of PVA can regulate the pore size of TiO_2 aerogels. Since the pore sizes of Ti-1, Ti-2 and Ti-3 are different and all belong to the mesoporous range, they were selected as photocatalysts and the Ti-0 was set as the

 doi:10.20944/preprints202405.1440.v1

control group to study the effect of pore size of TiO_2 aerogel on catalytic decomposition of formaldehyde.

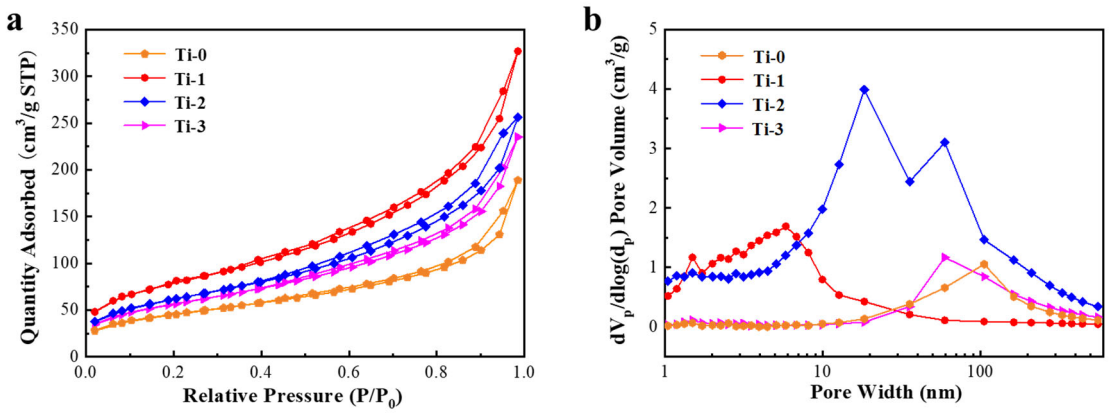

Figure 2. (a) N_2 adsorption-desorption curve and (b) pore size distribution of TiO_2 aerogels.

To explore the PVA content in the TiO_2 aerogel that had not been combined with TBOT, thermogravimetric analysis (TGA) was performed on the aerogel before being heated to 800 ℃ (as shown in Figure 3a). During the heating process, a considerable loss of mass was observed at temperatures ranging from 50-150°C. That was attributed to part of the water and ethanol solution would be retained in the mesopores of the TiO_2 aerogels during the drying process due to capillary coalescence. The Ti-1 aerogel, which had the smallest pore size, showed the most significant mass loss, while the Ti-2 and Ti-3 aerogels had less solution retention and lower mass loss as the capillary effect was reduced. PVA begins to decompose at 200~350°C, among which the maximum thermal weight loss of Ti-3 is 0.223 %, while the minimum is Ti-0 (0.033 %). When the TG temperature exceeded 400°C, the mass of the aerogel no longer changed, at which time the mass stabilization state had been reached. The results also indicated that not all PVA in TiO_2 was crosslinked with the hydrolyzed solution, in which the PVA remaining in the TiO_2 pores would all decompose and provide larger pore size for the TiO_2 aerogel after heat treatment at 300°C.

Further, Fourier transform infrared spectroscopy (FT-IR) was utilized to detect the chemical bonding of the TiO_2 aerogel after heat treatment at 800°C. As shown in Figure 3b, absorption peaks appeared at 950 cm^{-1} and 1072 cm^{-1}, which is corresponded to the characteristic vibration peak of Ti-O-Ti. The high frequency region of the spectra does not detect any vibrational peaks, indicating that the PVA in the heat-treated TiO_2 aerogel has been completely decomposed. Then the light absorption performance of TiO_2 aerogels were tested (Figure 3c). All four samples exhibited excellent light absorption in the UV wavelength region of 10-400 nm, which was consistent with the properties of TiO_2 aerogels photocatalysts. X-ray diffraction (XRD) tests conducted on TiO_2 aerogels after heat treatment at 800°C. As shown in Figure 3d, a series of crystal peaks at 2θ = 25°, 38°, 48°, 55°, 63° are corresponded to the (101), (004), (200), (211) and (204) lattice plane (PDF #71-1168). All the crystal structures are anatase, which may explain the excellent photocatalytic performance of the aerogels.

 doi:10.20944/preprints202405.1440.v1

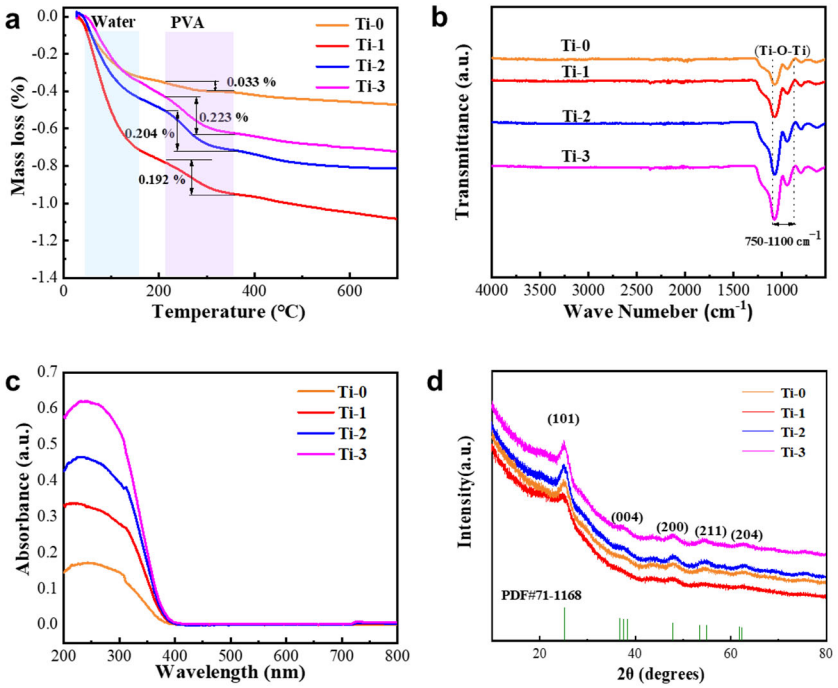

Figure 3. (a) The TGA curve, (b) FT-IR spectra, (c) UV absorption spectra and (d) XRD of TiO_2 aerogels.

3.2. Morphology Characterization of TiO_2 Aerogels

The transmission electron microscopy (TEM) tests were conducted to further confirm the crystal structure of TiO_2 aerogels shown in Figure 4. The images clearly show crystal lattice fringe with a spacing of 0.35 nm, corresponding to the (101) lattice plane of anatase crystal, consistent with the results obtained from XRD analysis (Figure 3d). According to the literature, the (101) lattice plane of anatase has excellent photocatalytic performance, which provides a basis decompose HCHO by as-prepared TiO_2 aerogels. As seen in Figure S_1, TiO_2 particle clusters were formed through nanoparticle cross-linking, with pores between the clusters. Among them, the pore size of Ti-1 was about 10 nm, which was smaller than that of Ti-2 (12.9 nm) and Ti-3 (48.6 nm). TiO_2 aerogel in Figure S_1(a_2, b_2, c_2) presents particles of about 3-6 nm, and these nanoparticles are cross-linked with each other, forming a porous network structure of TiO_2 aerogel. The distribution of nanoparticles in Ti-1 is relatively uniform, and there is no particle aggregation phenomenon, while the aggregation of nanoparticles in Ti-3 is obvious.

The scanning electron microscope (SEM) analysis provided further characterization of Ti-1, Ti-2, and Ti-3 microstructures. All samples displayed porosity as shown in Figure 4 (a_2-c_3). Ti-1 exhibited a relatively uniform particle distribution with no signs of particle aggregation, as shown in Figure 4 (a_2, b_2, c_2). Conversely, Ti-3 showed severe particle aggregation, consistent with TEM results. This could be attributed to cross-linking and entanglement of molecular chains due to increased of PVA content and aggregation of TiO_2 particles after high-temperature heat treatment. Consequently, the porosity of TiO_2 aerogels decreased significantly, and the pore sizes distribution became non-uniform. Meanwhile, Figure 4 (a_3, b_3, c_3) indicated that the pore sizes of all three TiO_2 aerogels were mesoporous, and these results are consistent with the data derived from the pore size distribution curves (Figure 2b) and the average pore size (Table S_1). Figure S_2 (a, b) shows the SEM of TiO_2 aerogel (Ti-0) without PVA. It can be seen in the Figure S_2 (a), the aggregation of nanoparticles in Ti-0 is obvious, and the pore sizes of Ti-0 ranging from 50-100 nm Figure S_2 (b).

 doi:10.20944/preprints202405.1440.v1

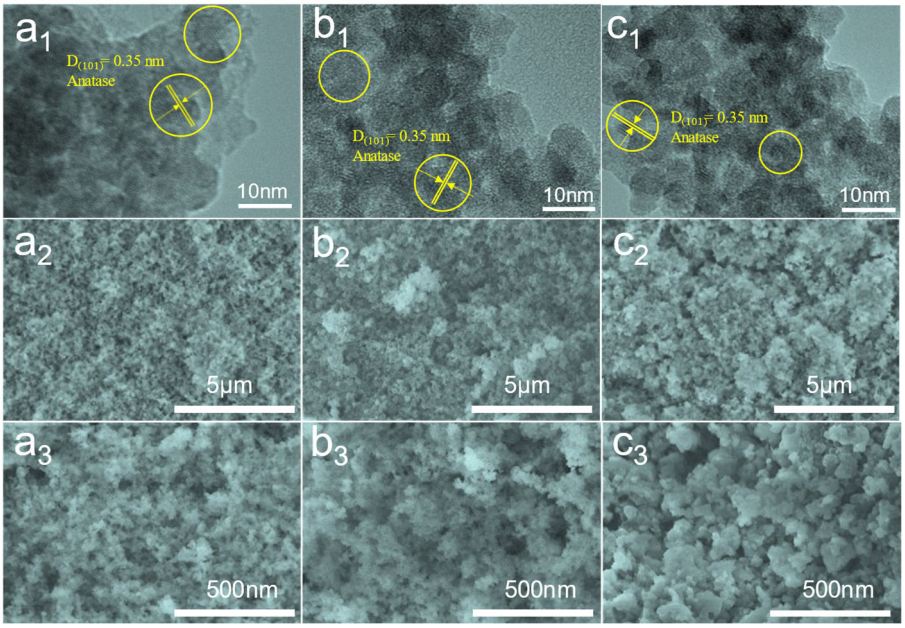

Figure 4. TEM images of sample (a_1) Ti-1, (b_1) Ti-2 and (c_1) Ti-3; SEM images of sample (a_2 a_3) Ti-1, (b_2 b_3) Ti-2 and (c_2 c_3) Ti-3.

3.3. Characterization of Photocatalytic Properties

Aerosols are defined as particulate matter with a diameter exceeding 0.01μm among atmospheric pollutants, while gaseous pollutants refer to those with a diameter below 0.01μm. VOCs typically combine with mineral aerosols for further migration and transformation. When formaldehyde gas volatilizes into the air and combines with aerosols, it results in an augmentation of particle size, thereby impeding the adsorption and decomposition of formaldehyde by TiO_2 aerogel. If the aerosol particle size is too large to enter the mesoporous of aerogel, hinder the decomposition of formaldehyde. Consequently, surface modification of the aerogel is necessary to disrupt the aerosol structure and facilitate formaldehyde molecule release for subsequent degradation. In this experiment, the degradation effect of aerogel on formaldehyde molecules was initially taken into account.

The photocatalytic decomposition experiments were carried out in a sealed volumetric bottle as illustrated in Figure S_3. As the HCHO aqueous solution volatilizes, a gas-liquid balance is reached in the bottle. When exposed to UV-light, TiO_2 aerogel breaks down HCHO in the gas, disrupting the gas-liquid balance of the solution and causing the HCHO to continue to volatilize, resulting in changes in the concentration of HCHO in the solution. The absorbance of HCHO aqueous solution was measured by UV spectrophotometer, and the absorption peak of HCHO aqueous solution was detected by gas chromatography (Figure 5). Aerogel in the mesoporous range, the absorption peak and absorbance of the HCHO aqueous solution containing Ti-1 were the lowest. Obviously, the GC results (Figure 5b) showed that the lowest HCHO signal was detected in Ti-1, while the relatively higher signal was observed in Ti-2. The measurement results were statistically measured and the standard uncertainties of all measurements were considered to obtain formaldehyde concentrations at different time points, as shown in Table (S_2, S_3, S_4). Compared with the original HCHO solution, Ti-1, Ti-2 and Ti-3 all demonstrated decomposition effects, but Ti-0 had almost no effect, which is caused by the average pore size of Ti-0 (64.6nm) belonged to the macroporous range (>50nm) rather than mesoporous (2-50nm). It can be seen from Table S_4 that Ti-1 possesses the more excellent catalytic effect. The above photocatalytic experimental results demonstrated that the pore size of TiO_2 aerogel has a significant effect on the photocatalytic degradation of HCHO. Based on the experimental results, the range of TiO_2 aerogel pore size with the best decomposition effect on HCHO was further determined by theoretical calculations.

Preprints.org (www.preprints.org) | NOT PEER-REVIEWED | Posted: 22 May 2024 doi:10.20944/preprints202405.1440.v1

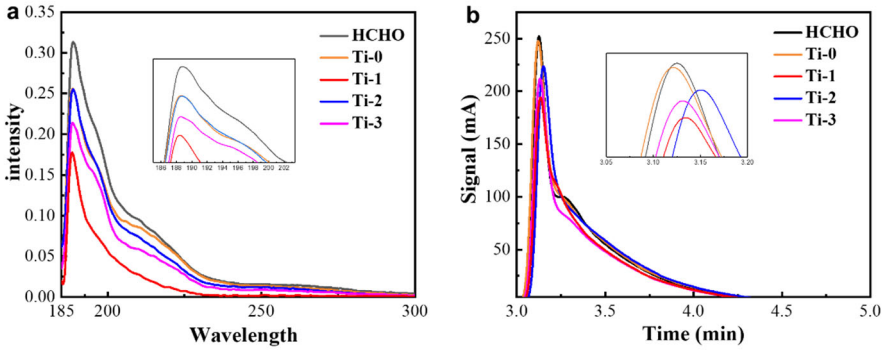

Figure 5. Absorption spectrum of (a) decomposed HCHO solution and (b) gas chromatographic absorption peak of HCHO solution.

3.4 Theoretical model and mechanism analysis

The photocatalytic decomposition of HCHO by TiO_2 was systematically investigated to elucidate the underlying mechanism. TiO_2 is a semiconductor that is composed of a valence band (VB) and a conduction band (CB), with the VB predominantly occupied by electrons and situated at the upper echelon, while the CB, characterized by electron vacancies, resides at the lower level. The energy disparity between the VB and the CB, known as the bandgap (Eg), delineates the forbidden gap. Under UV illumination, TiO_2 undergoes photonic excitation, generating electron-hole pairs, which play a pivotal role in the photocatalytic breakdown of HCHO. The sequence of reactions involved in the decomposition process [75,76], is detailed as follows:

$$TiO_2 + hv \rightarrow e^- + h\cdot^+$$
$$O_2 + e^- \rightarrow {O_2}^-$$
$$H_2O + h\cdot^+ \rightarrow \cdot OH + H^+$$
$$HCHO + (\cdot OH, {O_2}^-) \rightarrow CO_2 + H_2O$$

Upon UV illumination, TiO_2 surfaces initiate a photogenerated charge separation process, as illustrated in Figure 6. Electrons are excited from the VB to CB, where holes (h^+) are generated due to the loss of electrons in the VB, while the conduction band gains electrons (e^-), generating electron-hole pairs. The hole (h^+) located in the VB is oxidized with H_2O in the air to generate hydroxyl radicals (·OH) with strong oxidative capabilities, while the electron (e^-) at the conduction band reacts with O_2 to generate oxide anions (O^{2-}). These active substances engage in further reactions with HCHO, ultimately decomposing HCHO into CO_2 and H_2O. This result demonstrates that O_2 have participated in the photocatalytic HCHO decomposition process byTiO_2 and plays a key role during reaction.

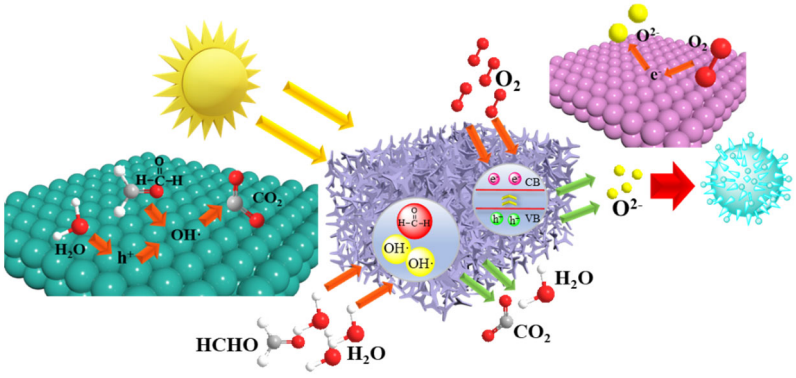

Figure 6. Reaction paths of O_2 and HCHO in TiO_2 aerogel pores.

To elucidate the role of O_2 in the photocatalytic process, we undertook a theoretical analysis, focusing on the pore sizes of the TiO_2 aerogels. The aerogel's porous structure encompasses a

 doi:10.20944/preprints202405.1440.v1

spectrum of pore sizes: micropores (diameter < 2nm), mesopores (diameter 2-50nm), and macropores (diameter > 50nm), with the TiO_2 aerogels in our samples predominantly featuring mesopores. The structural intricacies of the TiO_2 aerogel are depicted in Figure 7a, where a model showcases the intermolecular connections within the aerogels. This arrangement was modeled by considering the interconnections between TiO_2 molecules within the aerogel, resulting in the formation of TiO_2 clusters separated by different pore diameters. To more accurately represent the aerogel's environmental conditions, these pores were assumed to be air-filled, simulating the actual exposure scenario of the TiO_2 aerogel, illustrated in Figure 7b.

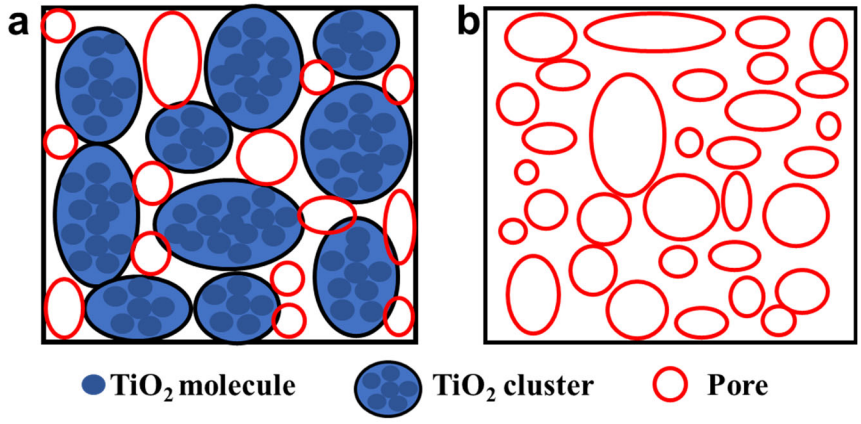

Figure 7. Distribution model of (a) cluster and (b) pore size in TiO_2 aerogel.

The existence of surface tension on the solid surface creates adsorption energy that effectively resists its effects, resulting in effective adsorption effect for liquid or gas molecules. Porous aerogels enhance this effect by continuously adsorbing multiple layers of water vapor molecules, leading to capillary condensation and a continuous gas liquefaction process. This generates an ultra-thin liquid layer on the solid surface of the pores, creating a gas-liquid interface with the gas in the pores (as shown in Figure 8a). TiO_2 aerogels exhibit the ability to adsorb multiple layers of water vapor molecules on the solid surface, forming a gas-liquid interface that conforms to the curvature of the solid. The influence of pore size on oxygen partial pressure was further investigated by simulating three pores with different curvatures, representing micropores, mesopores and macropores in TiO_2 aerogel, respectively, as illustrated in Figure S_4. Regardless of the different pore sizes, the number of layers of water vapor molecules that adsorb onto the surface remains the same. This leads to a continuous gas liquefaction process and subsequent capillary condensation. However, if the pore volume is larger, the liquid volume fraction occupying the hole is smaller, resulting in a greater volume fraction of gas (as depicted in Figure 8b). The content of water molecules in the pore of TiO_2 aerogel is related to the humidity of the air at room temperature and pressure. The larger pore size in a single pore corresponds to the larger surface area and the greater amount of adsorbed water molecules for O_2 production by photocatalysis. There are numerous active centers distributed on the surface of the aerogel, which play a catalytic role in decomposition process. When O_2 contacts the active center on the surface of the TiO_2 aerogel, electron transfer will occur between O_2 and TiO_2, which in turn promotes the catalytic reaction. In other words, the larger pore size can promote the catalytic reaction. However, the larger pore volume simultaneously means the lower oxygen pressure in the pore, thus resulting in the lower catalytic efficiency. Consequently, a relatively larger pore size can result in a decrease in the catalytic reaction. In summary, there is an optimal range of pore size in TiO_2 aerogel, which is conducive to the photocatalysis.

Preprints.org (www.preprints.org) | NOT PEER-REVIEWED | Posted: 22 May 2024 doi:10.20944/preprints202405.1440.v1

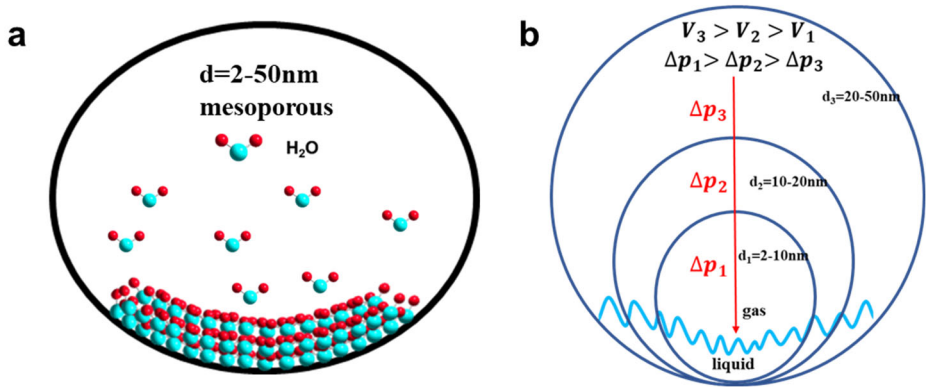

Figure 8. Schematic diagram of (a) adsorption-capillary condensation phenomenon and (b) oxygen pressure at the gas-liquid interface with different pore sizes in TiO_2 aerogel.

The reaction equation for HCHO decomposition is:

$$HCHO + O_2 = CO_2 + H_2O \tag{5}$$

For the reaction $mM + nN \rightarrow eE + fF$, the reaction rate equation is:

$$r_v = k[M]^m[N]^n \tag{6}$$

Where r_v is the reaction rate, k is the reaction rate constant, m and n are the series.

k is calculated according to the Arrhenius equation:

$$k = Aexp(-E_a/RT) \tag{7}$$

Where A is the Arrhenius constant; E_a is the Apparent activation energy (J/mol), and T is the thermodynamic temperature (K).

HCHO is decomposed to produce intermediate products, so the decomposition reaction process is a series of reactions

$$A_1 + A_2 \overset{k_1}{\rightarrow} B_1 + B_2 \overset{k_2}{\rightarrow} C_1 + C_2$$

For consecutive reactions, substances A (A_1, A_2) are reactants HCHO and O_2; substances B (B_1, B_2) are intermediate products, and the consumption and generation of substance B is occurred simultaneously; substances C (C_1, C_2) are products CO_2 and H_2O. so the equation of the rate of change of substance concentration is as follows:

$$-\frac{dc_{A1}}{dt} = k_1 c_{A1} c_{A2} \tag{8}$$

$$\frac{dc_{B1}}{dt} = k_1 c_{A1} c_{A2} - k_2 c_{B1} c_{B2} \tag{9}$$

$$\frac{dc_{C1}}{dt} = k_2 c_{B1} c_{B2} \tag{10}$$

The qualitative analysis of the calculated results only requires establishing the proportional relationship between r_v and c_A. so it is assumed that $c_{A1} = c_{A2}$.

Integral to draw, $c_{A1} = \frac{1}{\frac{1}{c_{A1,0}} + k_1 t} + C$

Where c_{A1} is concentration of substance A_1, $c_{A1,0}$ is initial concentration of substance A_1.

Therefore:

$$c_{HCHO} = \frac{1}{\frac{1}{c_{HCHO,0}} + k_1 t} + C \tag{11}$$

$$c_{O_2} = \frac{1}{\frac{1}{c_{O_2,0}} + k_1 t} + C \tag{12}$$

the reaction rate equation for HCHO decomposition is:

$$r_v = k[M]^m[N]^n = k_1 c_{HCHO} c_{O_2} = \left(\frac{1}{\frac{1}{c_{HCHO,0}} + k_1 t}\right)\left(\frac{1}{\frac{1}{c_{O_2,0}} + k_1 t}\right) + C \tag{13}$$

According to formula (13), reaction rate r_v is positively correlated with $c_{HCHO,0}$. A higher the O_2 concentration leads to a faster the reaction rate. According to Le Chatelier's principle, the

 doi:10.20944/preprints202405.1440.v1

concentration of the reaction gas increases, and the reaction proceeds in the direction of gas reduction. Hence, the reaction proceeds in the forward direction with the increases of O_2 concentration, resulting in the decomposition of HCHO.

Due to the surface of the pore in TiO_2 has the ability to absorb water molecules in the air, these molecules are directly contact with O_2 decomposed by TiO_2 catalysis, then participated in the catalytic decomposition of HCHO on TiO_2 aerogels. Therefore, according to the formula $S = 4\pi r^2$, (where S is surface area, r is radius) the decomposition reaction and the pore surface area were positively correlated. The decomposition reaction is proportional to the square of r. Conversely, as the pore size increases, the volume fraction occupied by gas also increased, resulting in the decrease of the oxygen partial pressure. According to the ideal gas equation $pV=nRT$, (where p is pressure, V is volume, n is amount of substance) the oxygen pressure is inversely proportional to the third power of the pore size r. In conclusion, O_2 pressure is inversely proportional to the pore size r of TiO_2 aerogel, that is, the larger pore size will lead to the smaller O_2 pressure (Figure 9).

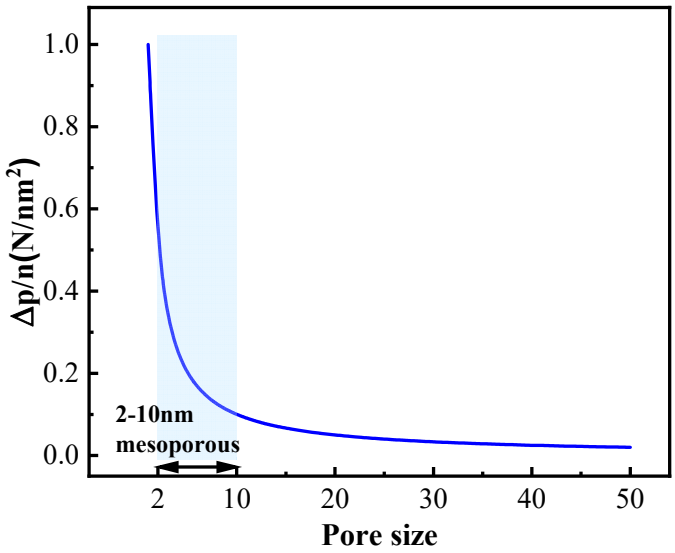

Figure 9. Relationship between pore size and O_2 pressure in TiO_2 aerogel.

As depicted in Figure 9, within the range mesoporous pores between 2 nm-50 nm, O_2 pressure decreases with the increase of pore size. In particular, with the mesoporous pores between 2 nm-10 nm, a pronounced rapid decrease in O_2 pressure is observed. Conversely, for pores exceeding 10 nm, this decrease becomes more gradual. Therefore, the pore size with the greatest influence on oxygen partial pressure in TiO_2 aerogel falls within the 2 nm to 10 nm range. According to formula (13), when the concentration of HCHO is determined, the concentration of O_2 has a decisive effect on the decomposition rate of HCHO. According to the above calculation results, the optimal pore size range of TiO_2 aerogel for HCHO photodecomposition is 2 nm~10 nm.

This investigation not only furnishes a novel theoretical framework for employing TiO_2 aerogels in HCHO decomposition reactions but also heralds new avenues for exploration in the realm of green chemistry, leveraging TiO_2 aerogels' unique properties.

4. Conclusions

TiO_2 aerogels with different pore sizes were prepared by sol-gel method, and flexible molecular chains were introduced by adding PVA to regulate the pore sizes of TiO_2 aerogels. TiO_2 aerogels prepared by adding PVA with mass fraction of 1%, 3% and 5% had an average pore size of 7.3 nm, 12.9 nm and 48.6 nm, respectively, and the pore size of TiO_2 aerogel without PVA was 64.6nm. The

 doi:10.20944/preprints202405.1440.v1

samples were characterized by FT-IR, UV and XRD, the structure and composition were almost the same. But the photocatalytic performance for HCHO decomposition of TiO_2 aerogels were tested by ultraviolet spectrophotometer and gas chromatography. Results show that the efficiency of decomposition of formaldehyde varies greatly, and the TiO_2 aerogels with an average pore size of 7.3 nm (Ti-1) had the highest HCHO decomposition efficiency, while the TiO_2 aerogels with Ti-0 shown the worst performance. Therefore, the pore size of TiO_2 aerogel, as the only variable, had a great effect on the decomposition of formaldehyde. To explore the relationship between pore size and HCHO decomposition efficiency, we established a theoretical model and verified that the decomposition efficiency of HCHO is related to the oxygen pressure in the pores of TiO_2 aerogel. Through derivation and calculation, the reaction rate equation of HCHO decomposition was obtained. The oxygen pressure is inversely proportional to the pore size r of TiO_2 aerogel, which indicate that the larger pore size is corresponded to the smaller oxygen pressure. Finally, the optimal pore size range of TiO_2 aerogel for HCHO photodecomposition is determined to be 2 nm~10 nm. This provides a theoretical idea for the application of TiO_2 aerogels and even porous materials in the field of catalytic decomposition.

Supplementary Materials: The following supporting information can be downloaded at: https: //www.mdpi.com/article/95.1002/polym5389243/s1, Figure S_1: TEM images of sample (a_1, a_1) Ti-1, (b_1, b_1) Ti-2 and (c_1, c_1) Ti-3; **Figure S_2** SEM images of sample (a, b) Ti-0; Figure S_3 Photocatalytic decomposition of HCHO by TiO_2 aerogel, from left to right are Ti-0, Ti-1, Ti-2 and Ti-3; Figure S_4 Adsorption of water molecules by TiO_2 aerogel with different pore sizes. Table S_1 Textural properties of TiO_2 aerogels; Table S_2 Standard uncertainty introduced in the measurement process; Table S_3 The values of formaldehyde concentration at different points in time; Table S_4 Multiple measurement data and standard uncertainty of experimental results.

Author Contributions: Data curation, F. S.; Formal analysis, X. Y.; Funding acquisition, J. X.; Investigation, F. S.; Methodology, F. S. and J. X.; Supervision, J. X.; Writing – original draft, F. S. All authors have read and agreed to the published version of the manuscript.

Funding: This research was funded by National Construction Program of First-Class University and First-Class Discipline(111800XX62).

Institutional Review Board Statement: Not applicable.

Data Availability Statement: Data are contained within the article and supplementary materials.

Acknowledgments: The work is supported by National Construction Program of First-Class University and First-Class Discipline and the Project of Novel Aerogel Materials Supported by Superel Advanced Materials Technology Co. Ltd.

Conflicts of Interest: The authors declare no conflict of interest financial or otherwise.

References

1. Cao, S.L.; Yeung, K.L.; Yue, P.L. Preparation of freestanding and crack-free titania–silica aerogels and their performance for gas phase, photocatalytic oxidation of VOCs. *Applied Catalysis B Environmental*, **2006**, *68*(3-4), 99-108. [CrossRef]
2. Li, X.W.; Li, H.W.; Huang, Y.; Cao, J.J.; Huang, T.T.; Li, R.; Zhang, Q.; Lee, S.C.; Ho, W.K. Exploring the photocatalytic conversion mechanism of gaseous formaldehyde degradation on TiO_{2-x}-OV surface. *Journal of Hazardous Materials*, **2022**, *424*(A), 127217. [CrossRef]
3. Song, MT.; Wu, YH.; Du, CF.; Su, YG. S-scheme bismuth vanadate and carbon nitride integrating with dual-functional bismuth nanoparticles toward co-efficiently removal formaldehyde under full spectrum light. *Journal of Colloid and Interface Science*, **2021**, *588*, 357-368. [CrossRef]
4. Lin, WS.; Zheng, JX.; Yan, LH.; Zhang, XX. Sol-gel preparation of self-cleaning SiO_2-TiO_2/SiO_2-TiO_2 double-layer antireflective coating for solar glass. *Results in Physics*, **2018**, *8*, 532-536. [CrossRef]
5. Yang, LX.; Guo, JW.; Yang, TQ.; Guo, C.; Zhang, SQ.; Luo, SL.; Dai, WL.; Li, B.; Luo, XB.; Li, Y. Self-assembly Cu_2O nanowire arrays on Cu mesh: A solid-state, highly-efficient, and stable photocatalyst for toluene degradation under sunlight. Journal of Hazardous Materials, 2021, 402, 123741. [CrossRef]
6. Duan, C.M.; Meng, M.W.; Huang, H.; Wang, H.; Ding, H.; Zhang, Q. Adsorptivity and kinetics for low concentration of gaseous formaldehyde on bamboo-based activated carbon loaded with ammonium acetate particles. *Environmental Research*, **2023**, *222*, 115364. [CrossRef]

7. Belaissaoui, B.; Le Moullec, Y.; Favre, E. Energy efficiency of a hybrid membrane/condensation process for VOC (Volatile Organic Compounds) recovery from air: A generic approach. Energy, 2016, 95, 291-302. [CrossRef]
8. Zhang, C.; Gao, X.; Qin, JC.; Guo, QK.; Zhou, HL.; Jin, WQ. Microporous polyimide VOC-rejective membrane for the separation of nitrogen/VOC mixture. *Journal of Hazardous Materials*, **2021**, *402*, 123817. [CrossRef]
9. Chen, YS.; Hsu, YC.; Lin, CC.; Tai, CYD.; Liu, HS. Volatile organic compounds absorption in a cross-flow rotating packed bed. *Environmental Science & Technology*, **2008**, *42*(7), 2631-2636. [CrossRef]
10. Shah, RK.; Thonon, B.; Benforado, DM. Opportunities for heat exchanger applications in environmental systems. *Applied Thermal Engineering*, **2000**, *20*(7), 631-650. [CrossRef]
11. Nian, H.J.; Meng, Q.C.; Zhang, W.; Chen, L.M. Overexpression of the formaldehyde dehydrogenase gene from brevibacillus brevis to enhance formaldehyde tolerance and detoxification of tobacco. *Applied Biochemistry and Biotechnology*, **2013**, *169*(1), 170-180. [CrossRef]
12. Mohamed, E.F.; Awad, G.; Ibrahim, A.S.S. Biodegradation of formaldehyde gas pollutant by a novel immobilized haloalkaliphilic Salipaludibacillus agaradhaerens strain NRC-R isolated from hypersaline soda lakes. *Results in Engineering*, **2023**, *19*, 101374. [CrossRef]
13. Kumar, V.; Lee, YS.; Shin, JW.; Kim, KH.; Kukkar, D.; Tsang, YF. Potential applications of graphene-based nanomaterials as adsorbent for removal of volatile organic compounds. *Environment International*, **2020**, *135*, 105356. [CrossRef]
14. Fan, X.; Zhu, T.L.; Sun, Y.F.; Yan, X. The roles of various plasma species in the plasma and plasma-catalytic removal of low-concentration HCHO in air. *Hazard Mater*, **2011**, *196*, 380-385. [CrossRef]
15. Wang, F.P.; Li, W.; Zhang, W.M.; Ye, R.R.; Tan, XH. Facile fabrication of the Ag nanoparticles decorated graphitic carbon nitride photocatalyst film for indoor air purification under visible light. *Building and environment*, **2022**, *222*, 109402. [CrossRef]
16. Kwon, DW.; Seo, PW.; Kim, GJ.; Hong, SC. Characteristics of the HCHO oxidation reaction over Pt/TiO_2 catalysts at room temperature: The effect of relative humidity on catalytic activity. *Applied Catalysis B: Environmental*, **2015**, *163*, 436-443. [CrossRef]
17. Sabia, P.; Romeo, F.; de Joannon, M.; Cavaliere, A. VOC destruction by water diluted hydrogen mild combustion. *Chemosphere*, **2007**, *68*(2), 330-337. [CrossRef]
18. Yang, CT.; Miao, G.; Pi, YH.; Xia, QB.; Wu, JL.; Li, Z.; Xiao, J. Abatement of various types of VOCs by adsorption/catalytic oxidation: A review. Chemical Engineering Journal, 2019, 370, 1128-1153. [CrossRef]
19. Zhang, K.; Ding, HL.; Pan, WG.; Mu, XT.; Qiu, KN.; Ma, JC.; Zhao, YT.; Song, J.; Zhang, ZY. Research progress of a composite metal oxide catalyst for VOC degradation. *Environmental Science & Technology*, **2022**, *56*(13), 9220-9236. [CrossRef]
20. Liang, W.J.; Li, J.; Jin, Y.Q. Photo-catalytic degradation of gaseous formaldehyde by TiO_2/UV, Ag/TiO_2/UV and Ce/TiO_2/UV. *Building and Environment*, **2012**, *51*, 345-350. [CrossRef]
21. Ding, JY.; Yang, YJ.; Liu, J.; Wang, Z. Catalytic reaction mechanism of formaldehyde oxidation by oxygen species over Pt/TiO_2 catalyst. *Chemosphere*, **2020**, *248*, 125980. [CrossRef]
22. Khaki, MRD.; Shafeeyan, MS.; Raman, AAA.; Daud, WMAW. Application of doped photocatalysts for organic pollutant degradation - A review. *Journal of Environmental Management*, **2017**, *198*, 78-94. [CrossRef]
23. Ahmad, R.; Ahmad, Z.; Khan, AU.; Mastoi, NR.; Aslam, M.; Kim, J. Photocatalytic systems as an advanced environmental remediation: Recent developments, limitations and new avenues for applications. *Journal of Environmental Chemical Engineering*, **2016**, *4*(4, Part A), 4143-4164. [CrossRef]
24. Rao, Z.P.; Lu, G.H.; Chen, L.; Mahmood, A.; Shi, G.S.; Tang, Z.X.; Xie, X.F.; Sun, J. Photocatalytic oxidation mechanism of Gas-Phase VOCs: Unveiling the role of holes, ·OH and $\cdot O^{2-}$. *Chemical Engineering Journal*, **2022**, *430*(2), 132766. [CrossRef]
25. Backus, E.H.G.; Hosseinpour, S.; Ramanan, C.; Sun, S.M.; Schlegel, S.J.; Zelenka, M.; Jia, X.Y.; Gebhard, M.; Devi, A.; Wang, H.I.; Bonn, M. Ultrafast surface-specific spectroscopy of water at a photoexcited TiO_2 model water-splitting photocatalyst. *Angewandte Chemie-International Edition*, **2024**, *63*(8), 2312123. [CrossRef]
26. Li, J.Y.; Cui, W.; Chen, P..; Dong, X.A.; Chu, Y.H.; Sheng, J.P.; Zhang, Y.X.; Wang, Z.M.; Dong, F. Unraveling the mechanism of binary channel reactions in photocatalytic formaldehyde decomposition for promoted mineralization. *Applied Catalysis B-Environmental*, **2020**, *260*, 118130. [CrossRef]
27. Chen, H.H.; Nanayakkara, C.E.; Grassian, V.H. Grassian. Titanium dioxide photocatalysis in atmospheric chemistry. *Chemical Reviews*, **2012**, *112*(11), 5919-5948. [CrossRef]
28. Wang, WJ.; Lin, FW.; An, TC.; Qiu, SX.; Yu, HD.; Yan, BB.; Chen, GY.; Hou, LA. Photocatalytic mineralization of indoor VOC mixtures over unique ternary TiO_2/C/MnO_2 with high adsorption selectivity[J]. *Chemical Engineering Journal*, **2021**, *425*, 131678. [CrossRef]
29. Huang, H.B.; Ye, X.G.; Huang, H.L.; Zhang, L.; Leung, D.Y.C. Mechanistic study on formaldehyde removal over Pd/TiO_2 catalysts: oxygen transfer and role of water vapor. *Chemical Engineering Journal*, **2013**, *230*, 73-79. [CrossRef]

30. Li, Y.B.; Chen, X.Y.; Wang, C.Y.; Zhang, C.B.; He, H. Sodium enhances Ir/TiO_2 activity for catalytic oxidation of formaldehyde at ambient temperature. *ACS Catalysis*, **2018**, *8*(12), 11377-11385. [CrossRef]
31. Wang, X.D.; Zhang, K.; Guo, X.L.; Shenb, G.D.; Xiang, J.Y. Synthesis and characterization of N-doped TiO_2 loaded onto activated carbon fiber with enhanced visible-light photocatalytic activity. *New Journal of Chemistry*, **2014**, *38*(12), 6139-6146. [CrossRef]
32. Cheng, X.W.; Yu, X.J.; Xing, Z.P.; Wan, F.; Yang, G. Enhanced photocatalytic activity of nitrogen doped TiO_2 anatase nano-particle under simulated sunlight irradiation. *Energy Procedia*, **2012**, *16*(A), 598-605. [CrossRef]
33. Liu, W.X.; Jiang, P.; Shao, W.N.; Zhang, J.; Cao, W.B. A novel approach for the synthesis of visible-light-active nanocrystalline N-doped TiO_2 photocatalytic hydrosol. *Solid State Sciences*, **2014**, *33*, 45-48. [CrossRef]
34. Tompsett, G.A.; Bowmaker, G.A.; Cooney, R.P.; Metson, J.B.; Rodgers, K.A.; Seakins, J.M. The Raman spectrum of brookite, TiO_2 (Pbca, Z=8). *Journal of Raman Spectroscopy*, **1995**, *26*(1), 57-62. [CrossRef]
35. Yue, X.; Xiang, J.H.; Chen, J.Y.; Li, H.X.; Qiu, Y.S.; Yu, X.B. High surface area, high catalytic activity titanium dioxide aerogels prepared by solvothermal crystallization. *Journal of Materials Science & Technology*, **2020**, *47*, 223-230. [CrossRef]
36. Cao, S.L.; Yeung, K.L.; Kwan, J.K.C.; To, PMT.; Yu, S.C.T. An investigation of the performance of catalytic aerogel filters. *Applied Catalysis B-Environmental*, **2009**, *86*(3-4), 127-136. [CrossRef]
37. Chen, W.; Sui, L.X.; Long, X.; Liao, J.X.; Wang, S.Z.; Wei, X.B. Anatase TiO_2 aerogel with high specific surface areas and porous network structures for ultra-fast response hydrogen sensor. *International Journal of Hydrogen Energy*, **2024**, *50*, 973-991. [CrossRef]
38. Li, FZ.; Gao, S.; Niu, YT.; Song, JB.; Zhao, WX.; Niederberger, M.; Cheng, W. Large-scale synthesis of macroscopic layered inorganic-organic hybrid nanobelt aerogel monoliths with multifunctionality. *Cell Reports Physical Science*, **2022**, *3*(10), 101079. [CrossRef]
39. Zhou, TP.; Xu, YT.; Zhen, Y.; Wu, KJ.; Ding, HH.; Wang, LJ.; Tai, XL.; Cai, XR.; Zhang, X.; Xia, TP.; Zhu, JF.; Chu, WS.; Ni, Y.; Xie, Y.; Wu, CZ. Layered inorganic silicate aerogel pillared by nanoclusters for high temperature thermal insulation. *Advanced Materials*, **2023**, *35*(49), 2306135. [CrossRef]
40. Kim, Y.N.; Shao, G.N.; Jeon, S.J.; Imran, S.M.; Sarawade, P.B.; Kim, H.T. Sol–gel synthesis of sodium silicate and titanium oxychloride based TiO_2-SiO_2 aerogels and their photocatalytic property under UV irradiation. *Chemical Engineering Journal*, **2013**, *231*, 502-511. [CrossRef]
41. Zhao, SY.; Malfait, WJ.; Jeong, EH.; Fischer, B.; Zhang, YC.; Xu, HX.; Angelica, E.; Risen, WM.; Suggs, W.; Koebel, MM. Facile one-pot synthesis of mechanically robust biopolymer silica nanocomposite aerogel by cogelation of silicic acid with chitosan in aqueous media. *Acs Sustainable Chemistry & Engineering*, **2016**, *4*(10): 5674-5683. [CrossRef]
42. Oschatz, M.; Nickel, W.; Thommes, M.; Cychosz, KA.; Leistner, M.; Adam, M.; Mondin, G.; Strubel, P.; Borchardt, L.; Kaskel, S. Evolution of porosity in carbide-derived carbon aerogels. *Journal of Materials Chemistry A*, **2014**, *2*(43), 18472-18479. [CrossRef]
43. Noman, M.T.; Ashraf, M.A.; Ali, A. Synthesis and applications of nano-TiO_2: a review. *Environmental Science and Pollution Research*, **2019**, *26*(4), 3262-3291. [CrossRef]
44. Li, X.; Dong, GQ.; Liu, ZW.; Zhang, XT. Polyimide aerogel fibers with superior flame resistance, strength, hydrophobicity, and flexibility made via a universal sol-gel confined transition strategy. *Acs Nano*, **2021**, *15*(3), 4759-4768. [CrossRef]
45. Prokic-Vidojevic, D.; Glisic, SB.; Krstic, JB.; Orlovic, AM. Aerogel Re/Pd-TiO_2 SiO_2 and Co/Mo-Al_2O_3 SiO_2 catalysts for hydrodesulphurisation of dibenzothiophene and 4,6-dimethyldibenzothiophene. *Catalysis Today*, **2021**, *378*, 10-23. [CrossRef]
46. Lamy-Mendes, A.; Malfait, WJ.; Sadeghpour, A.; Girao, AV.; Silva, RF.; Duraes, L. Influence of 1D and 2D carbon nanostructures in silica-based aerogels. *Carbon*, **2021**, *180*, 146-162. [CrossRef]
47. Alavi, F.; Ciftci, ON. Developing dual nano/macroporous starch bioaerogels via emulsion templating and supercritical carbon dioxide drying. *Carbohydrate Polymers*, **2022**, *292*, 119607. [CrossRef]
48. Trinh, T.T.P.N.X.; Giang, N.T.H.; Huong, L.M.; Thinh, D.B.; Dat, N.M.; Trinh, D.N.; Hai, N.D.; Oanh, D.T.Y.; Nam, H.M.; Phong, M.T.; Hieu, N.H. Hydrothermal synthesis of titanium dioxide/graphene aerogel for photodegradation of methylene blue in aqueous solution. *Journal of Science-Advanced Materials and Devices*, **2022**, *7*(2), 100433. [CrossRef]
49. Wu, QS.; Sun, H. Preparation and properties of porous ceramics from nickel slag by aerogel gelcasting. *Ceramics International*, **2022**, *48*(22), 33058-33065. [CrossRef]
50. Coles, M.P.; Lugmair, C.G.; Terry, K.W.; Tilley, T.D. Titania-silica materials from the molecular precursor $Ti[OSi(O^tBu)_3]_4$:: Selective epoxidation catalysts. *Chemistry of Materials*, **1999**, *12*(1), 122-131. [CrossRef]
51. Xiao, H.; Yang, MR.; Lv, JB.; He, X.; Chen, MH.; Tan, W.; Yang, WJ.; Zeng, K.; Hu, JH.; Yang, G. Biomineralization-inspired confined-space fabrication of polyimide aerogels. *Acs* Applied *Materials & Interfaces*, **2024**, *16*(2), 2763-2773. [CrossRef]

52. Yang, X.; Ma, J.J.; Ling, J.; Li, N.; Wang, D.; Yue, F.; Xu, S.M. Cellulose acetate-based SiO_2/TiO_2 hybrid microsphere composite aerogel films for water-in-oil emulsion separation. *Applied Surface Science*, **2018**, *435*(MAR.30), 609-616. [CrossRef]
53. Jia, HJ.; Liu, S.; Mao, ZY.; Wang, DJ. Preparation and properties of the Al_2O_3-SiO_2 aerogel/alumina framework composite. *Ceramics International*, **2021**, *47*(1): 1466-1471. [CrossRef]
54. Giang, N.T.H.; Tan, N.N.; Huong, L.; Hai, N.D.; Thinh, N.T.; Phuc, N.T.; Dat, N.M.; Phong, M.T.; Hieu, N.H. Photocatalytic degradation of crystal violet on titanium dioxide/graphene aerogel doped sulfur. *Journal of Molecular Structure*, **2023**, 1271, 134031. [CrossRef]
55. Abdullah, HB.; Irmawati, R.; Ismail, I.; Yusof, NA. Utilization of waste engine oil for carbon nanotube aerogel production using floating catalyst chemical vapor deposition. *Journal of Cleaner Production*, **2020**, *261*, 121188. [CrossRef]
56. Ye, XL.; Chen, ZF.; Ai, SF.; Hou, B.; Zhang, JX.; Zhou, QB.; Wang, F.; Liu, HZ.; Cui, S. Microstructure characterization and thermal performance of reticulated SiC skeleton reinforced silica aerogel composites. *Composites Part B-Engineering*, **2019**, *177*, 107409. [CrossRef]
57. Zhou, XP.; Wang, YF.; Xiao, LJ.; Zhang, MY.; Su, ZA.; Huang, QZ. Preparing carbon black aerogel quickly by chemical vapor deposition. *Composites Communications*, **2023**, *37*, 101460. [CrossRef]
58. Doneliene, J.; Fataraite-Urboniene, E.; Danchova, N.; Gutzov, S.; Ulbikas, J. The influence of the precursor's nature and drying conditions on the structure, morphology, and thermal properties of TiO_2 aerogels. *Gels*, **2022**, *8*(7), 422. [CrossRef]
59. Doneliene, J.; Fataraite-Urboniene, E.; Rudzikas, M.; Pakalka, S.; Danchova, N.; Ulbikas, J. Effect of precursor nature and sol-gel synthesis conditions on TiO_2 aerogel's structure. *Molecules*, **2021**, *26*(16), 5059. [CrossRef]
60. Feng, Q.G.; Cai, H.D.; Lin, H.Y.; Qin, S.Y.; Liu, Z.; Ma, D.C.; Ye, Y.Y. Synthesis and structural characteristics of high surface area TiO_2 aerogels by ultrasonic-assisted sol–gel method. *Nanotechnology*, **2018**, *29*(7), 050702. [CrossRef]
61. Somjit, V.; Thinsoongnoen, P.; Sriphumrat, K.; Pimu, S.; Arayachukiat, S.; Kongpatpanich, K. Metal-organic framework aerogel for full ph range operation and trace adsorption of arsenic in water. *Acs Applied Materials & Interfaces*, **2022**, *14*(35), 40005-40013. [CrossRef]
62. Su, X.P.; Liao, Q.; Liu, L.; Meng, R.J.; Qian, Z.Q.; Gao, H.Y.; Yao, J.M. Cu_2O nanoparticle-functionalized cellulose-based aerogel as high-performance visible-light photocatalyst. *Cellulose*, **2017**, *24*(2), 1017-1029. [CrossRef]
63. Habibi, S.; Jamshidi, M. Synthesis of TiO_2 nanoparticles coated on cellulose nanofibers with different morphologies: Effect of the template and sol-gel parameters. *Materials Science in Semiconductor Processing*, **2020**, *109*, 104927. [CrossRef]
64. Konuk, OP.; Alsuhile, AAAM.; Yousefzadeh, H.; Ulker, Z.; Bozbag, SE.; García-González, CA.; Smirnova, I.; Erkey, C. The effect of synthesis conditions and process parameters on aerogel properties. *Frontiers in Chemistry*, **2023**, *11*, 1294520. [CrossRef]
65. Rebber, M.; Sannemüller, H.; Jaruszewski, M.; Pfannkuche, D.; Urakawa, A.; Koziej, D. Light and mass transport computations guide the fabrication of 3D-structured TiO_2 and Au/TiO_2 aerogel photocatalysts for efficient hydrogen production in the gas phase. *Chemistry of Materials*, **2023**, *35*(10), 3849-3858. [CrossRef]
66. Dong, G.L.; Gao, Y.B.; Chen, S.Y. Effects of different drying methods on the properties of TiO_2 particles. *Acta Physico-Chimica Sinica*, **1998**, *14*(2), 142-146. [CrossRef]
67. Liu, J.X.; Bai, L.N.; Shi, F.; Hu, Z.Q.; Jiang, Y.Y.; Zhao, T. Pore structure characterization of TiO_2-SiO_2 composite aerogel prepared via ambient pressure drying by sol pre-modification process. *Advanced Materials Research*, **2012**, *534*, 101-105. [CrossRef]
68. Moussaoui, R.; Elghniji, K.; ben Mosbah, M.; Elaloui, E.; Moussaoui, Y. Sol-gel synthesis of highly TiO_2 aerogel photocatalyst via high temperature supercritical drying. *Journal of Saudi Chemical Society*, **2017**, *21*(6), 751-760. [CrossRef]
69. Ghosal, S.; Baumann, T.F.; King, J.S.; Kucheyev, S.O.; Wang, Y.M.; Worsley, M.A.; Biener, J.; Bent, S.F.; Hamza, A.V. Controlling atomic layer deposition of TiO_2 in aerogels through surface functionalization. *Journal of Immunology*, **2009**, *183*(10), 6619-6628. [CrossRef]
70. Xia, Y.; Man, J.W.; Wu, X.D.; Huang, S.T.; Lu, A.Q.; Shen, X.D.; Cui, S.; Chen, X.B.; Fu, G.T. Oxygen-vacancy-assisted construction of Ce–TiO_2 aerogel for efficiently boosting photocatalytic CO_2 reduction without any sacrifice agent. *Ceramics International*, **2023**, *49*(4), 6100-6112. [CrossRef]
71. Zu, G.Q.; Shen, J.; Wang, W.Q.; Zou, L.P.; Lian, Y.; Zhang, Z.H. Silica-titania composite aerogel photocatalysts by chemical liquid deposition of titania onto nanoporous silica scaffolds. *Acs Appl Mater Interfaces*, **2015**, *7*(9), 5400-5409. [CrossRef]
72. Li, S.T.; Li, G.; Chen, Q.; Wang, F. Facile green synthesis of degraded-PVA coated TiO_2 nanoparticles with enhanced photocatalytic activity under visible light. *Journal of Physics and Chemistry of Solids*, **2019**, *129*, 92-98. [CrossRef]

 doi:10.20944/preprints202405.1440.v1

73. Li, L.S.; Yang, G.D.; Lyu, J.; Sheng, Z.Z.; Ma, F.G.; Zhang, X.T. Folk arts-inspired twice-coagulated configuration-editable tough aerogels enabled by transformable gel precursors. *Nature Communications*, **2024**, *14*(1), 8450. [CrossRef]
74. Xue, T.T.; Zhu, C.Y.; Feng, X.L.; Wali, Q.; Fan, W.; Liu, TX. Polyimide Aerogel Fibers with Controllable Porous Microstructure for Super-Thermal Insulation Under Extreme Environments. *Advanced Fiber Materials*, **2022**, *4*(5), 1118-1128. [CrossRef]
75. Rasalingam, S.; Wu, C.M.; Koodali, R.T. Modulation of pore sizes of titanium dioxide photocatalysts by a facile template free hydrothermal synthesis method: implications for photocatalytic degradation of rhodamine B. *Acs Appl Mater Interfaces*, **2015**, *7*(7), 4368-4380. [CrossRef]
76. Shayegan, Z.; Lee, C.S.; Haghighat, F. TiO_2 photocatalyst for removal of volatile organic compounds in gas phase – A review. *Chemical Engineering Journal*, **2017**, *334*, 2408-2439. [CrossRef]